Sensors & Actuators: B. Chemical 471 (2027) 141052

Contents lists available at ScienceDirect

Sensors and Actuators: B. Chemical

journal homepage: www.elsevier.com/locate/snb

Geo-inspired nanogaps for back-excited flexible SERS and deep-learning-enabled multiplexed molecular sensing

Seunghyun Lee [a,1], Minki Kim [b,1], Joonho Lee [a,1], Changhyun Choi [a], Seungyeop Ryu [b], Jinhyeok Yang [b], Yeonhong Kim [a,*], Junseong Ahn [b,*], Wooyoung Lee [a,*]

[a] Department of Materials Science and Engineering, Yonsei University, Seoul, 03722, Republic of Korea
[b] Department of Control and Instrumentation Engineering, Korea University, Sejong, 30019, Republic of Korea

ARTICLE INFO

Keywords:
Flexible SERS substrate
Crack engineering
Backside excitation
Deep learning
On-body sensing
Pesticide detection

ABSTRACT

Practical SERS on real-world surfaces faces an optical-access problem: when the plasmonic face of a conventional front-excitation flexible substrate is placed in contact with the sample, the hotspot layer becomes difficult to illuminate and collect from the same side without disturbing the analyte–substrate interface. Beyond this geometric constraint, reliable interpretation of complex multi-analyte spectra requires data-efficient classification. Here we report a geo-inspired nanogap platform based on a hierarchical crack network integrating backside SERS with deep-learning-enabled molecular analysis. A sequential mechanothermal process, comprising uniaxial strain, cryogenic-thermal treatment, and sonication, generates a dense, hierarchical crack network on an Ag/PDMS bilayer. This yields a ~150-fold increase in the averaged experimental SERS intensity relative to bare Ag, while FDTD simulations show that the spatially averaged electromagnetic enhancement increases from 1.9×10^2 for MS only to 7.5×10^3 for MS + CT + S, with a consistent backside intensity advantage preserved across all processing stages. Coupling this hardware to 1D-CNN classifiers trained on synthetic mixtures enables multi-analyte screening without the need for exhaustive empirical mixture data. The platform is therefore intended primarily for multiplexed molecular identification and screening rather than generalized quantitative concentration determination. We demonstrate the platform through label-free detection of pesticide residues on fruit surfaces and co-existing sweat metabolites from collected perspiration samples, providing a scalable pathway for multiplexed point-of-care and food-safety monitoring.

1. Introduction

Surface-enhanced Raman scattering (SERS) is increasingly applied to on-site and on-body chemical analysis [1–3]. In these settings, performance depends not only on the strength of the electromagnetic hotspot, but also on how conformally the substrate contacts the sample interface [4]. Food surfaces are rough, wet or curved; biofluids such as sweat and tears are scarce and continuously renewed; and living tissues are auto fluorescent and mechanically compliant [5,6]. A practical SERS substrate must therefore maintain intimate contact with irregular or soft surfaces [5–7].

Over the past five decades, SERS substrates have progressed from rigid metal films and colloidal nanoparticles to paper-based sensors, optical fibres, dried-spot arrays, elastomer films and skin-attachable patches [2,8]. Many of these platforms, however, rely on lithographic patterning, colloidal self-assembly or multi-step chemical synthesis, which complicates large-area fabrication [9,10]. Although crack-based, wrinkled, and flexible SERS substrates have expanded the available strategies for generating plasmonic hotspots and achieving conformal sample contact, representative approaches still rely on nanoparticle assembly, predefined lithographic structures, or predominantly two-dimensional surface crack or wrinkle geometries; transparent backside-sensing platforms likewise require separate substrate nanostructuring or repeated metal deposition and annealing [11–15]. Most reported platforms also operate under front-side excitation, in which the laser path and analyte layer are located on the same side of the substrate. In real-world contact measurements, however, placing the plasmonic layer against the sample makes the sample-facing hotspots difficult to access using same-side excitation and collection. Consequently, the analyte is typically drop-cast onto the hotspot layer, or the substrate is

* Corresponding authors.
E-mail addresses: menong91@yonsei.ac.kr (Y. Kim), junseong@korea.ac.kr (J. Ahn), wooyoung@yonsei.ac.kr (W. Lee).
[1] These authors contributed equally

https://doi.org/10.1016/j.snb.2026.141052
Received 6 July 2026; Received in revised form 19 September 2026; Accepted 6 October 2026
Available online 10 October 2026
0925-4005/© 2026 Elsevier B.V. All rights are reserved, including those for text and data mining, AI training, and similar technologies.

pressed against and then detached from the target before measurement [16–18]. Both protocols can disturb the native interface and redistribute analytes before measurement.

A further challenge arises from the spectral complexity of real-world samples. Sweat, fruit peel, meat surfaces and other field-relevant matrices contain multiple co-existing molecules with overlapping Raman fingerprints, accompanied by baseline drift and matrix-dependent background signals [19,20]. Because spectral features of individual components overlap in such mixtures, single-peak identification is no longer sufficient and data-driven classification is instead required [21,22]. In practice, however, acquiring large labeled datasets of real multi-analyte mixtures is prohibitively time-consuming [21, 23–26]. A scalable training strategy must therefore generate diverse synthetic mixture-like spectra from a limited library of single-analyte references, using preprocessing and augmentation steps that account for instrumental variability and background variation [25,26]. Practical multi-analyte SERS therefore requires the sensing substrate and spectral-analysis pipeline to be designed together rather than optimized in isolation.

In this Article, we report a geo-inspired nanogap platform based on a hierarchical crack network that integrates backside SERS with deep-learning-enabled multiplexed molecular analysis. The design is guided

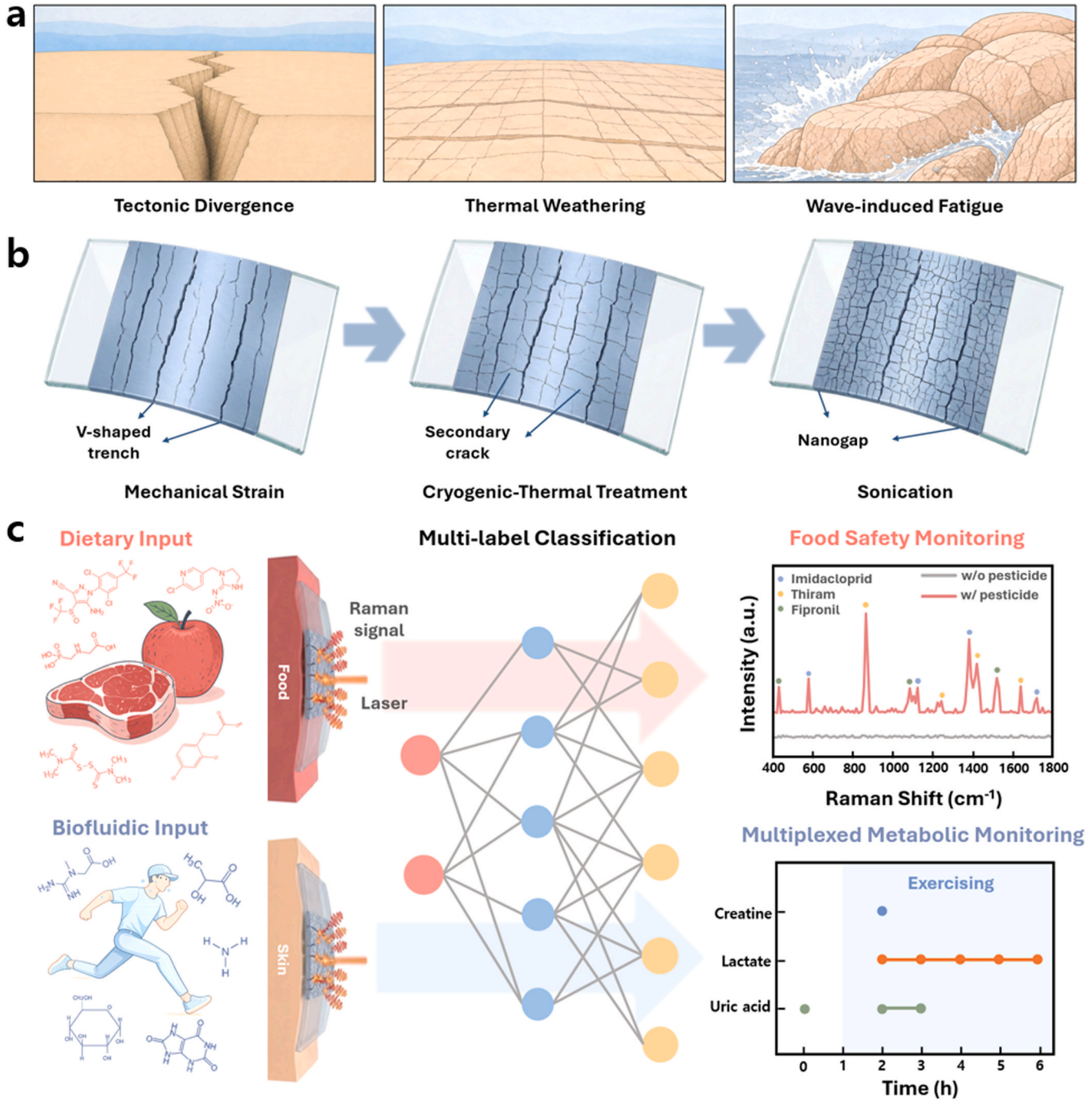


Fig. 1. Geo-inspired nanogap platform based on a hierarchical crack network for backside SERS and multiplexed molecular sensing. a, Geological motifs of tectonic divergence, thermal weathering and wave-induced fatigue used as design templates for crack formation. b, Translation into an Ag/PDMS bilayer via mechanical strain, cryogenic–thermal treatment and sonication, producing hierarchical crack network from the micro- to the nanoscale. c, Backside SERS detection coupled to a deep-learning model for multiplexed analysis of food and biofluid samples.

by three geological motifs that generate fracture networks in nature: tectonic divergence, thermal weathering and wave-driven mechanical fatigue (Fig. 1a). These motifs are implemented as sequential crack-engineering steps: uniaxial mechanical strain generates directional cracks in the Ag/PDMS bilayer, cryogenic–thermal treatment expands the crack network through the Ag/PDMS thermal-expansion mismatch and sonication introduces nanoscale surface cracking. Through this sequential process, the Ag/PDMS bilayer evolves into a hierarchical crack network comprising V-shaped trenches, secondary cracks, and nanogaps (Fig. 1b). This process directly generates SERS-active nanogaps from the deposited Ag film without nanoparticle synthesis and self-assembly or direct lithographic definition of individual nanogaps. Although strain-induced trench formation and patterned V-shaped SERS structures have separately been reported [27,28], neither study combines post-treatment-assisted densification of strain-induced V-shaped trenches with enhanced backside SERS interrogation. To the best of our knowledge, this is the first demonstration of a backside-enhanced SERS platform based on strain-induced V-shaped trenches. The novelty therefore lies in the fabrication process and resulting measurement architecture, while the underlying enhancement remains the established LSPR-mediated electromagnetic mechanism at metallic nanogaps [29]. Individual processing steps and their combined effects are characterized by morphological imaging, shear-lag and thermomechanical analysis, and three-dimensional finite-difference time-domain simulations. The platform further integrates the acquired SERS spectra with two task-specific one-dimensional convolutional neural network (1D-CNN) classifiers: a single-label classifier for targeted single-analyte identification and a multi-label classifier for screening co-existing analytes (Fig. 1c). Accordingly, the primary objective of this study is to establish a SERS-based platform for multiplexed molecular identification and screening using chemically distinct spectral fingerprints and deep-learning classification. To overcome the scarcity of labeled mixture data, the training pipeline expands a compact single-analyte reference library through spectral augmentation and linear-superposition-based synthesis of mixture-like spectra, supporting multiplexed molecular analysis without exhaustive mixture-by-mixture data collection. As demonstrations, the integrated platform addresses food-surface and biofluid-relevant molecular sensing, targeting pesticide residues on fruit and resolving co-existing sweat metabolites at complex sample interfaces.

2. Results and discussion

2.1. Mechanism-based sequential crack engineering and hierarchical morphology

The hierarchical crack network comprises distinct structural features that emerge sequentially during processing. Mechanical strain forms V-shaped trenches with a residual Ag layer connected at the trench bottom, whereas cryogenic–thermal treatment and sonication generate fully separated secondary cracks and narrower nanogaps, respectively. These features are distinguished here according to their cross-sectional morphology and fabrication stage; detailed definitions and classification criteria are provided in Supplementary Note 1 and Supplementary Fig. 1.

Inspired by tectonic divergence, where tensile separation opens directional cracks, uniaxial tensile loading was used as the first crack-engineering step in the Ag/PDMS bilayer. Because simple mechanical stretching does not readily yield stable nanoscale gaps, this step was designed to create a tapered V-shaped trench framework that can be partially closed after strain release and refined into hierarchical crack network. Under uniaxial tensile loading, the Ag/PDMS bilayer (Ag 50 nm; PDMS ~300 μm) generates a periodic array of V-shaped trenches oriented perpendicular to the loading direction (Fig. 2a), and focused-ion-beam cross-sectional imaging confirms a characteristic V-shaped trench geometry with the opening width largest at the Ag free surface and gradually narrowing towards the Ag/PDMS interface (Fig. 2b). Following a shear-lag description, the inter-crack spacing scales with the stress-transfer length of the bilayer (Eq. S1, S2 and Supplementary Note 2) [30–34]. After strain release, elastic recovery of the PDMS reduces the strain-induced crack openings, leaving stable V-shaped trenches [35,36].

Quantitative imaging across applied strains of 15–75% (Supplementary Fig. 1b and Supplementary Table 2) shows that the periodicity of the V-shaped trenches decreases monotonically from ~30 μm to ~4 μm, indicating progressive crack multiplication with increasing pre-strain. At 75% strain, the vertical trench period measured across six independent plan-view SEM images follows a distribution with a mean ± SD of 4.77 ± 1.42 μm (N = 36; Supplementary Fig. 3 and Supplementary Table 3). At the optimized 75% strain, cross-sectional STEM imaging reveals representative tapered V-shaped trench, with a top opening of ~100 nm and a localized nanoscale bottom opening of ~10–20 nm (Supplementary Fig. 1b). This geometry is consistent with post-release narrowing of strain-induced V-shaped trenches through PDMS elastic recovery, as discussed in Supplementary Note 2. This progressive densification of the crack network is directly reflected in the SERS response: SERS intensity, measured by Raman mapping of Rhodamine 6 G (R6G, 10^{-5} M), increases monotonically with applied strain (Supplementary Fig. 4 and Fig. 2c), and backside excitation consistently exceeds front-side excitation, reaching ~1.7-fold at 75% strain (Supplementary Fig. 6); the origin of this directional asymmetry is examined in the following section. Tensile strains above 75% consistently promoted Poisson-contraction-driven horizontal cracking, as exemplified by the 90% strain case in Supplementary Fig. 5. At high pre-strain, these horizontal cracks locally interrupted the vertical trench-crack network and formed wide defect regions that are less favorable for nanoscale near-field coupling (Supplementary Fig. 5 and Supplementary Note 2) [32,34]. Thus, 75% served as the upper strain limit.

Inspired by thermal weathering, where rapid temperature variations propagate fractures from pre-existing defects, cryogenic–thermal treatment was introduced as the second crack-engineering step to expand the mechanically generated V-shaped trenches. When the same cryogenic–thermal cycle was applied to a pristine, unstrained Ag/PDMS film, no additional cracks formed (Fig. 2d). In contrast, applying the cycle to the released MS-treated Ag/PDMS substrate generated a dense network of secondary cracks branching from V-shaped trenches (Fig. 2e). This control establishes that the pre-existing V-shaped trenches act as stress concentrators and traction-free boundaries that lower the critical stress for thermally driven fracture (Eq. S3, S4 and Supplementary Note 3) [37–41]. The 100 °C upper annealing limit was selected to promote crack reopening and interconnection through thermal hysteresis while suppressing Ag dewetting or nanoisland formation, preserving the structural continuity of the plasmonic layer [37,41,42]. The combined MS + CT process yields markedly stronger SERS enhancement than either mechanical strain or cryogenic–thermal treatment alone (Fig. 2 f), confirming the synergistic role of the secondary crack network.

As the final refinement step, sonication was used to mimic wave-driven mechanical fatigue, in which repeated hydrodynamic impacts progressively erode and fracture pre-existing structures. Although the preceding mechanical strain and cryogenic–thermal steps establish the microscale crack network, the crack surfaces remain relatively smooth at the nanoscale, limiting hotspot density. Sonication in ethanol introduces nanoscale features onto the pre-formed Ag/PDMS crack network without disrupting its global morphology (Fig. 2 g). Acoustic cavitation produces high-velocity microjets whose impulsive pressures, on the order of 10–100 MPa (Eq. S5 and Supplementary Note 4) [43–45], are comparable to the yield strength of ultrathin Ag films [46,47]. The Ag layer is particularly susceptible to such loading because of its low bending stiffness, which scales as t^3 for a thin plate (Eq. S6); consequently, the 50-nm Ag layer can undergo repeated local out-of-plane deflection under these cavitation impacts [48,49]. Pre-existing crack edges and narrow Ag ligaments act as mechanically

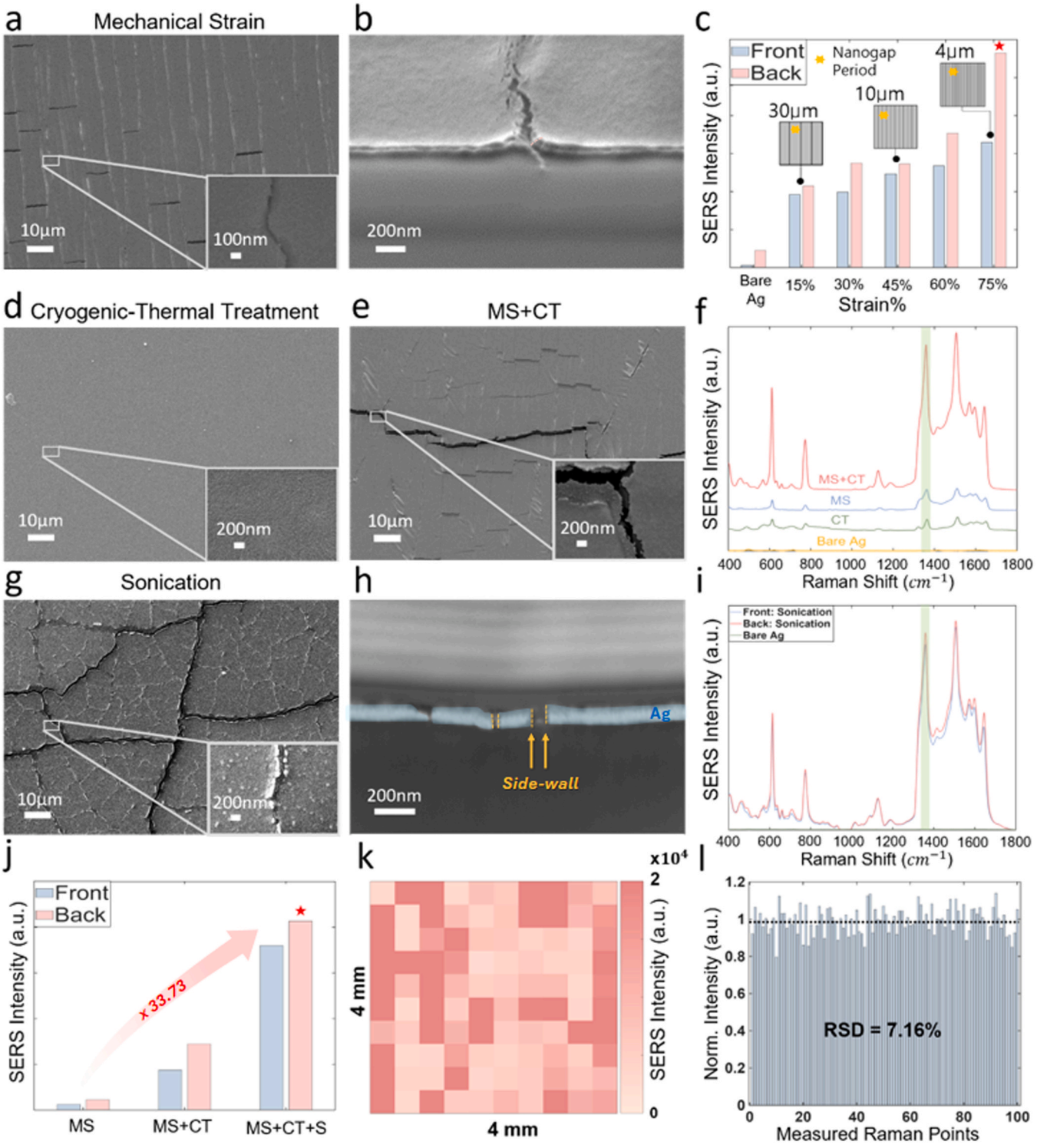


Fig. 2. Mechanism-based sequential crack engineering and SERS performance. **a**, SEM image of strain-induced V-shaped trenches in the Ag/PDMS bilayer; inset, enlarged top-view of a representative V-shaped trench. **b**, FIB-SEM cross-sectional image of the V-shaped trench. **c**, SERS intensity and V-shaped trench period as a function of applied tensile strain (15–75%) under front-side and backside excitation. **d**, SEM image of the Ag/PDMS surface after cryogenic–thermal (CT) treatment without pre-existing cracks. **e**, SEM image of the secondary crack network after sequential mechanical strain and cryogenic–thermal treatment (MS+CT); inset, high-magnification view. **f**, SERS spectra comparing CT only, MS only and combined MS + CT conditions. **g**, SEM image of sonication-induced nanoscale surface features on the MS + CT network; inset, high-magnification view. **h**, FIB-SEM cross-sectional image of nanogaps formed by sonication only, showing nearly straight-walled, symmetric profiles. **i**, Front-side and backside SERS spectra after sonication only (S). **j**, Comparison of SERS intensity for MS, MS + CT and MS + CT + S substrates under front-side and backside excitation. **k**, Backside Raman intensity map over a 4 × 4 mm^2 area for the MS + CT + S substrate. **l**, Spot-to-spot relative standard deviation (RSD = 7.16%) of the normalized backside SERS intensity.

vulnerable sites where stress concentration and cyclic bending accumulate fatigue-like damage, promoting nanoscale roughening and nanogap formation while largely preserving the overall hierarchical crack network [33,34]. FIB-SEM cross-sections reveal that sonication-only nanogaps are nearly straight-walled (Fig. 2 h), presenting a symmetric optical environment to the two excitation directions. Accordingly, when sonication is applied as a standalone process to a pristine Ag/PDMS film, the resulting SERS enhancement is essentially identical under front- and backside excitation (Fig. 2i). In contrast, sonication applied to the MS + CT-treated substrate further increases the SERS response while the backside intensity advantage is preserved (Fig. 2j). Because the two cases differ only in the presence or absence of the tapered V-shaped trench, this control experiment provides direct experimental evidence that the directional backside enhancement originates from the asymmetric trench geometry rather than from nanoscale roughening alone. This result confirms that the sonication step selectively enhances hotspot density without erasing the strain-defined geometric asymmetry, whose detailed morphology is examined in the following section.

The three steps act synergistically rather than additively (Fig. 2j). Mechanical strain alone produces a ~5-fold enhancement relative to bare Ag through V-shaped trenches; cryogenic–thermal treatment alone yields only a ~3-fold enhancement, consistent with the absence of new fracture; and the sequential combination of mechanical strain followed by cryogenic–thermal treatment yields a ~30-fold enhancement, confirming activation of the secondary network only on the pre-existing strain-crack scaffold. The fully combined mechanical strain + cryogenic–thermal + sonication (MS+CT+S) process reaches a ~150-fold enhancement, a further ~5-fold gain over MS + CT, and the backside advantage is preserved across all stages. The averaged intensity was obtained from spectra collected at 100 positions over a 4 × 4 mm^2 area, as detailed in the SERS measurement protocol and Supplementary Fig. 10. The approximately 150-fold value is therefore an experimentally measured relative intensity ratio rather than an experimental or

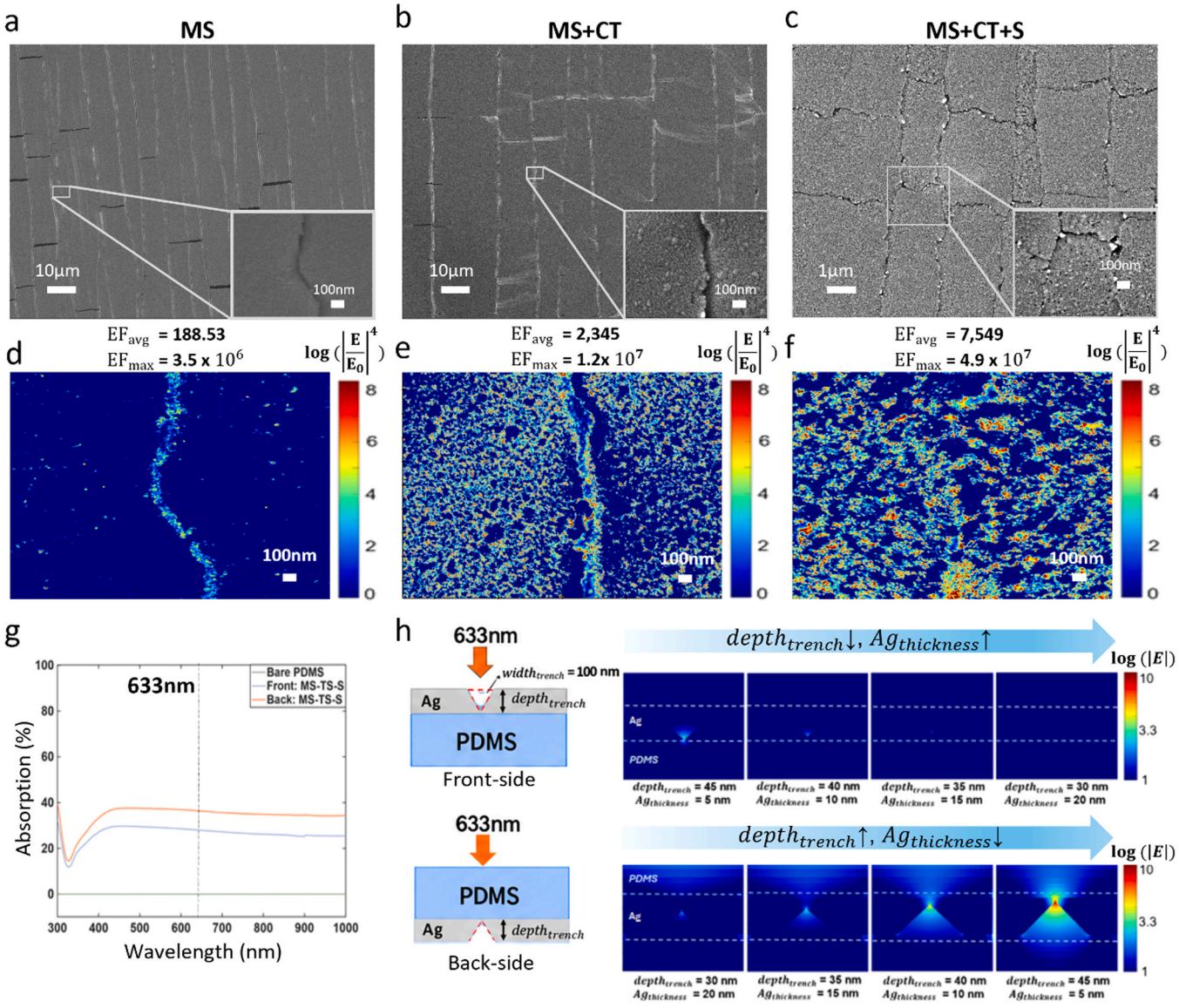


Fig. 3. Optical characterization and electromagnetic field analysis of the nanogap SERS platform. a–c, SEM images of the surface morphology evolution across the sequential process stages: a, mechanical strain only (MS); **b**, mechanical strain + cryogenic–thermal treatment (MS+CT); **c**, the fully combined MS + CT + S process. Scale bars: 10 μm (a, b), 1 μm (c); insets, 100 nm. **d–f**, FDTD-simulated electric-field intensity maps ($\log|E/E_0|^4$, top view) at 633 nm corresponding to the morphologies in **a–c**. **g**, UV–Vis–NIR absorption spectra of the MS + CT + S substrate under front-side (orange) and backside (red) illumination, with bare PDMS (gray) as a reference. **h**, Cross-sectional FDTD electric-field profiles ($\log|E|$) within the V-shaped trench under front-side (upper row) and backside (lower row) excitation at 633 nm; the top opening is fixed at 100 nm and the trench depth is varied from 30 to 45 nm (residual Ag thickness 20–5 nm).

simulated SERS enhancement factor. Spatial uniformity, assessed by 100-point Raman mapping over a 4 × 4 mm^2 area under backside excitation (Supplementary Fig. 7), shows uniformly high enhancement without localized dead regions of weak enhancement (Fig. 2k). The spot-to-spot relative standard deviation of the normalized intensity is 7.16% (Fig. 2 l), satisfying the < 10% criterion widely used for reproducible SERS substrates[27] and providing the spectral consistency required for downstream learned classification.

2.2. Optical characterization and electromagnetic field analysis

To resolve the underlying plasmonic mechanism, experimental top-view SEM morphologies at each process stage (Fig. 3a-c) were imported as binary masks for three-dimensional finite-difference time-domain simulations, thereby avoiding idealized periodic geometries (Supplementary Note 5). Fig. 3d-f show the calculated electric-field intensity maps ($\log|E/E_0|^4$, top view) at 633 nm. Both the spatially averaged electromagnetic enhancement, EF_{avg}, and the maximum local electromagnetic enhancement, EF_{max}, were calculated. Because EF_{max} represents an isolated local field maximum rather than the response averaged over the experimentally sampled area, the processing-dependent comparison is based on EF_{avg}. The MS-only structure produces sparse hotspots along isolated V-shaped trenches (EF_{avg} of approximately 1.9 ×10^2). Adding the cryogenic-thermal step increases EF_{avg} to 2.3 × 10^3 as secondary cracks branch from the primary trenches. The fully combined MS + CT + S sample produces dense, uniformly distributed hotspots with EF_{avg} of 7.5 × 10^3 (Supplementary Table 4). Relative to MS only, EF_{avg} increases by approximately 12.4-fold after MS + CT and 40-fold after MS + CT + S. The averaged experimental SERS intensity shows the same increasing trend, rising by approximately sixfold and 30-fold, respectively, when normalized to the MS-only substrate. The numerical ratios are not expected to be identical because the FDTD simulation describes only the electromagnetic field distribution, whereas the experimental response also reflects the actual three-dimensional gap morphology, analyte distribution and spatial sampling. Nevertheless, both results consistently show that narrower gaps and increased hotspot density progressively increase the averaged SERS response.

Because SERS enhancement scales with the electromagnetic energy absorbed at the excitation wavelength [50,51], we measured UV–visible–NIR absorption spectra of the MS + CT + S substrate under both front-side and backside illumination, with bare PDMS as a reference (Fig. 3 g). The 300 μm-thick PDMS support exhibits high transmittance in the visible region, rendering scattering losses negligible upon backside illumination at 633 nm [52,53]. Bare PDMS exhibits negligible absorption (~0%) across 300–1000 nm, consistent with its transparency. The MS + CT + S-processed Ag/PDMS substrate shows broadband absorption across visible and near-infrared wavelengths under both illumination directions, but absorbs consistently more light under backside illumination. At the 633 nm SERS excitation wavelength, backside absorption reaches 36–37%, compared with 27–28% under front-side illumination, a ~9 %age-point advantage that correlates directly with the experimentally observed backside SERS intensity gain.

Cross-sectional simulations of the V-shaped trench under both excitation directions (top opening fixed at 100 nm; trench depth varied from 30 to 45 nm, corresponding to a residual Ag thickness of 20–5 nm; Fig. 3 h) clarify the directional asymmetry (Supplementary Fig. 8). Under front-side illumination, the field enhancement is concentrated near the wide top aperture and does not extend into the deeper trench region. In contrast, under backside illumination, substantially stronger and more deeply confined fields develop inside the trench, with the maximum intensity localized at the narrow bottom (~10–20 nm gap width). Two coupled effects account for this asymmetry (Supplementary Note 6): sub-skin-depth evanescent coupling through the thinned residual Ag at the trench bottom, which allows backside-incident light to excite gap-surface-plasmon-polariton (gap-SPP) modes directly at the narrowest section of the trench [54–58]; and sub-wavelength gap-SPP confinement that scales inversely with the gap width [55,57]. The V-shaped geometry underpins both effects and also governs the coupling asymmetry. Under backside excitation, the incident field arrives at the narrow gap where it overlaps efficiently with the confined gap-SPP mode. Under front-side excitation, by contrast, light enters the wide aperture where spatial overlap with the confined mode is poor and most energy is reflected consistent with the lower front-side absorption (27–28% vs 36–37% at 633 nm). These mechanisms are quantitatively consistent with the higher backside absorption and the experimentally observed backside SERS intensity advantage. Notably, under backside illumination both the excitation light and the Raman-scattered signal must traverse the thin residual Ag layer at the trench bottom, incurring a partial loss in each pass. Nevertheless, the substantially stronger gap-SPP coupling efficiency at the narrow trench base and the resulting near-field enhancement more than compensates for this double-pass attenuation, yielding a net backside SERS intensity that exceeds the front-side value.

2.3. SERS reproducibility and concentration-dependent analytical response of pesticides and biomarkers

To assess the analytical reproducibility of the MS + CT + S substrate at the level of individual measurements used in the subsequent quantitative analysis, the spot-to-spot uniformity reported in Fig. 2 l was further benchmarked at the inter-substrate scale. Raman spectra of R6G (10^{-5} M) were acquired at the center of twenty independently fabricated substrates following the same fabrication protocol, and the RSD at the 1361 cm^{-1} band across the twenty substrates was 7.2% (Fig. 4a-i). The corresponding waterfall plot of the twenty single-substrate spectra confirms that the characteristic R6G fingerprint is preserved across all independently fabricated samples (Fig. 4a-ii). This value falls below the 10% benchmark commonly cited for reproducible SERS substrates, indicating that the MS + CT + S platform retains spectral consistency from device to device even under backside illumination, where transmission through the PDMS support could in principle compromise reproducibility [59–61].

The R6G peak intensity at 1361 cm^{-1} increased monotonically with the incident laser power at the sample plane from 1 to 5.8 mW, whereas a further increase to 6.5 mW, the maximum available setting, produced only a marginal additional gain, indicating the onset of saturation (Fig. 4b). This saturation is consistent with the onset of photoinduced effects such as photobleaching of R6G or local photothermal heating at the nanogap hotspots, both of which limit further scaling of the SERS signal at higher incident power densities [62–67]. The standard acquisition power of 5.8 mW used throughout this work is therefore the highest setting at which the response had not yet saturated, and all spectra used for comparison and classification were acquired at this fixed power (Methods).

To characterize the concentration-dependent analytical response of the substrate, R6G spectra were acquired across three orders of magnitude in concentration, from 10^{-4} to 10^{-7} M (Fig. 4c-i). The characteristic peaks remained clearly resolvable down to 10^{-7} M, and the peak intensity at 1361 cm^{-1} scaled with concentration in the log-log scale, with the slope below unity that decreased gradually toward higher concentrations rather than following a direct proportionality (Fig. 4c-ii). Here, 10^{-7} M represents the lowest tested concentration at which the characteristic R6G peaks remained resolvable under the present measurement conditions and is not assigned as a statistically determined LOD. The same analysis was applied to thiram, a representative dithiocarbamate pesticide commonly encountered as a residue on fruit and vegetable surfaces, and the peak intensity at 1381 cm^{-1} exhibited a comparable saturating dependence over the same tested concentration range (Fig. 4c-iii). This concentration-dependent curvature, more pronounced for thiram, is consistent with adsorption-limited surface saturation, in

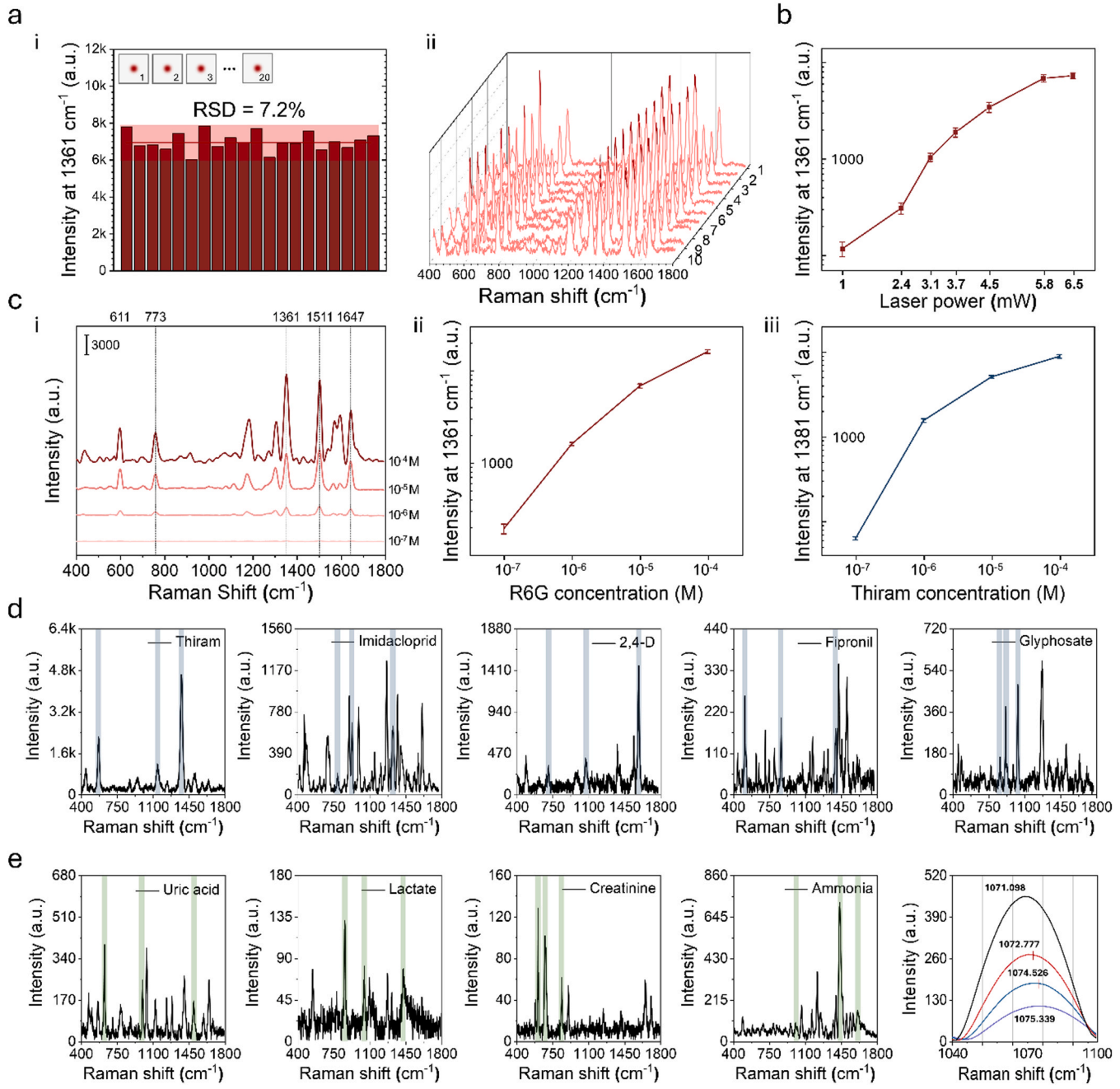


Fig. 4. SERS measurement uniformity and detection capability of the MS + CT + S substrate. a, Inter-substrate reproducibility evaluated by measuring R6G (10^{-5} M) on twenty independently fabricated substrates. **i,** RSD of the Raman intensity at 1361 cm^{-1} across the twenty substrates, yielding 7.2%; the schematic in the upper left indicates the inter-sample sampling protocol. **ii,** Corresponding Raman spectra of the twenty substrates, plotted as a waterfall. **b,** Dependence of the R6G (10^{-5} M) Raman intensity at 1361 cm^{-1} on the incident laser power at the sample plane from 1 to 6.5 mW, plotted with a logarithmic intensity axis; the intensity increases monotonically up to 5.8 mW and shows only a marginal further gain at 6.5 mW, indicating the onset of saturation. **c,** Concentration-dependent SERS response of R6G and thiram. **i,** Raman spectra of R6G at concentrations from 10^{-4} to 10^{-7} M, plotted with vertical offset for clarity. **ii,** Concentration dependence of the peak intensity at 1361 cm^{-1} as a function of R6G concentration on a log-log plot. **iii,** Concentration dependence of the peak intensity at 1381 cm^{-1} as a function of thiram concentration on a log-log plot. **d,** Reference SERS spectra (10^{-3} M) of five representative pesticides arranged left to right: thiram, imidacloprid, 2,4-D, fipronil and glyphosate. **e,** Reference SERS spectra of five sweat metabolites arranged left to right: uric acid, lactate, creatinine and ammonia at 10^{-3} M, followed by glucose measured in the 1040–1100 cm^{-1} region on a 4-MPBA functionalized MS + CT + S substrate at 0, 30, 100 and 150 μM, where the 4-MPBA ring-breathing peak shifts from 1071.1 cm^{-1} to 1072.8, 1074.5 and 1075.3 cm^{-1} with increasing glucose concentration. All measurements were carried out under backside excitation at 633 nm with a laser power of 5.8 mW at the sample plane (spot area 0.73 μm^2, power density ~8×10^5 W cm^{-2}) and 10 s integration time unless otherwise specified. In b, c-ii and c-iii, each data point is the mean of five spectra acquired at different positions of the same substrate and error bars denote the standard deviation.

which higher analyte concentrations progressively occupy the available nanogap hotspots until the response begins to plateau [68–70]. Despite this curvature, the response remains reproducible and concentration-dependent over the three orders of magnitude investigated, demonstrating a systematic analytical response across the tested concentration range.

A broader analyte panel relevant to the food-surface and biofluid scenarios targeted in this work was then surveyed. Reference spectra

(10^{-3} M) of thiram, imidacloprid, 2,4-D, fipronil and glyphosate (Fig. 4d) cover five representative pesticides routinely encountered as residues on agricultural produce, while spectra of uric acid, lactate, creatinine, ammonia and glucose (Fig. 4e) cover five principal sweat metabolites that report on hydration, exertion and renal status [71–73]. Among these, glucose was detected indirectly on a 4-mercaptophenylboronic acid (4-MPBA) functionalised substrate, where the 4-MPBA ring-breathing peak in the 1070–1080 cm^{-1} region progressively blue-shifts with increasing glucose concentration (0–150 μM) owing to boronate-ester formation between 4-MPBA and the diol moiety of glucose (Fig. 4e) [74]. Each analyte exhibits a distinct combination of fingerprint bands whose vibrational mode assignments are summarized in Supplementary Table 5, confirming that the substrate transduces molecular identity into spectra that are both reproducible and chemically specific across the pesticide and biomarker libraries assembled in this work. Together, these results show that the MS + CT + S substrate provides reproducible, sensitive, and chemically distinct SERS fingerprints suitable for downstream molecular identification and multiplexed classification.

2.4. Deep-learning analysis of single- and multi-analyte SERS spectra

While the substrate produces reproducible spectra with chemically distinct fingerprints, real biofluid and food-surface samples typically contain co-existing analytes whose Raman fingerprints partially overlap, and matrix-dependent fluorescence further obscures fine peak structure, making manual spectral interpretation inefficient [75–77]. Two task-specific 1D-CNN classifiers were therefore developed on top of the same substrate platform, a single-label classifier dedicated to targeted identification and quantitative concentration regression of a chosen analyte, and a multi-label classifier dedicated to screening for multiple co-existing analytes (Fig. 5).

To compensate for the limited number of measurements per analyte, fifty Raman spectra per pure substance were expanded through a two-branch pipeline that produced low-variation samples and high-variation samples (Fig. 5a). Low-variation samples reproduce the natural spot-to-spot variability of a high-quality measurement on the substrate and were generated through mild intensity scaling, small Raman shift perturbation, and small-amplitude Gaussian noise. High-variation samples instead represent measurements that are weak or unclear because of low local analyte coverage or non-ideal acquisition conditions, and were generated using the same operations over wider ranges that additionally include peak broadening. Full augmentation parameters are provided in Methods. The single-label classifier was trained on this augmented single-analyte set, partitioned into training, validation and test subsets at the level of the original measured spectra (Methods), without any mixture data. Augmentation was applied only after this partitioning and only to the measured spectra assigned to training, so that no augmented spectrum shares its original measurement with a validation or test spectrum.

For the multi-label classifier, virtual mixture spectra were synthesized by linear superposition of the augmented single-analyte spectra to approximate experimental mixtures without exhaustively measuring every combination. Because the broad background of a SERS spectrum differs between independently prepared samples, each measured spectrum was first converted to its Savitzky-Golay first derivative, which removes the additive background and slowly varying baseline contributions so that the network input is governed by the positions and shapes of the Raman bands rather than by the sample-specific background; augmentation and mixture synthesis were then carried out in this derivative representation, in which linear superposition remains valid (Methods). When the synthetic distribution is placed alongside the experimentally measured mixture distribution in Fig. 5a, the two distributions overlap closely, supporting the use of synthetic mixtures as training data. Fig. 5b validates the same assumption at the spectrum level by overlaying experimentally measured spectra of imidacloprid (i), thiram (ii), and a 1:1 imidacloprid + thiram mixture (iii); the measured mixture displays the diagnostic peaks of both single components in approximately additive form, confirming that summing two single-analyte spectra is a reasonable approximation of an experimental mixture spectrum within the working concentration range used here. Synthetic mixtures were generated for every pairwise combination of the five target analytes and for the ternary combination examined experimentally (thiram, imidacloprid and 2,4-D), with mixing coefficients spanning the full continuum from weakly visible to balanced and dominant components (regime ranges in Methods) so that the network was exposed to a broader range of dominance ratios than the balanced 1:1 case alone. The multi-label classifier was then trained on the union of the augmented single-analyte spectra and these synthetic mixtures.

Both classifiers share the same 1D-CNN backbone (Fig. 5c) but differ in their output design: a softmax head in the single-label classifier returns mutually exclusive class probabilities for targeted analyte identification, while a sigmoid head in the multi-label classifier returns independent presence probabilities for screening co-existing analytes (full layer configurations in Methods). Two single-label classifiers of identical architecture were trained separately on the pesticide panel (2,4-D, fipronil, glyphosate, imidacloprid, and thiram) and the biomarker panel (ammonia, creatinine, glucose, lactate, and uric acid), reaching a worst-class test accuracy of 96.7% for both panels (Figs. 5d-i and 5D-ii) on held-out spectra; the confusion matrices show only a small number of cross-class assignments, indicating that the 1D-CNN operates reliably on spectra acquired from the MS + CT + S platform.

Beyond categorical identification, the glucose channel was extended to quantitative concentration estimation by functionalising the Ag surface with 4-mercaptophenylboronic acid (4-MPBA), whose ring-breathing mode in the 1070–1080 cm^{-1} region shifts upon boronate-ester formation with glucose [78–80]. In a single spectrum of a 65 μM reference solution, the 4-MPBA peak was located at 1073.88 cm^{-1} (Fig. 5e-i), and when a measured spectrum was classified as glucose, the corresponding peak position was passed to a second-order calibration curve fitted to peak shift versus concentration; the regression model returned 67.47 μM for this measurement, corresponding to a relative error of 3.8% from the nominal 65 μM concentration (Fig. 5e-ii). This targeted regression is presented as an analyte-specific proof of concept enabled by 4-MPBA recognition chemistry and analyte-specific calibration and does not imply a universal quantitative capability across the multiplexed analytes.

Finally, the multi-label sigmoid network was evaluated on 105 experimentally acquired mixture spectra that were never used for training, validation or threshold selection: thiram + imidacloprid at nominal loading ratios of 1:1 (20 spectra), 1:2 (5) and 1:4 (5), the 1:1 mixture with R6G added as an untrained interferent (5), thiram + 2,4-D at 1:3 (35) and the ternary mixture thiram + imidacloprid + 2,4-D at 1:2:3 (35); the per-class confusion matrices for the thiram + imidacloprid conditions are shown in Fig. 5 f and the results for all conditions are summarized in Supplementary Table 6. The loading ratio denotes the number of sequential drop-cast applications of equal-concentration solutions, and thiram, the strongest SERS scatterer of the panel, was kept as the minority component so that the weaker scatterers dominated every mixture (Supplementary Fig. 12 and Methods). Class-specific decision thresholds were selected on the validation set by an F1 criterion (Supplementary Note 7). Every constituent analyte was identified in all 105 spectra, 104 spectra received exactly the correct set of labels, and fipronil and glyphosate, which were absent from every sample, were never flagged; the single deviation was an additional 2,4-D flag on one of the five R6G-containing spectra. The classifier thus maintained its multiplexed identification across different dominance ratios, across a binary and a ternary combination that it had never encountered as measured mixtures, and in the presence of an untrained interferent that contributes its own bands and a fluorescence background, without having seen any experimentally measured mixture

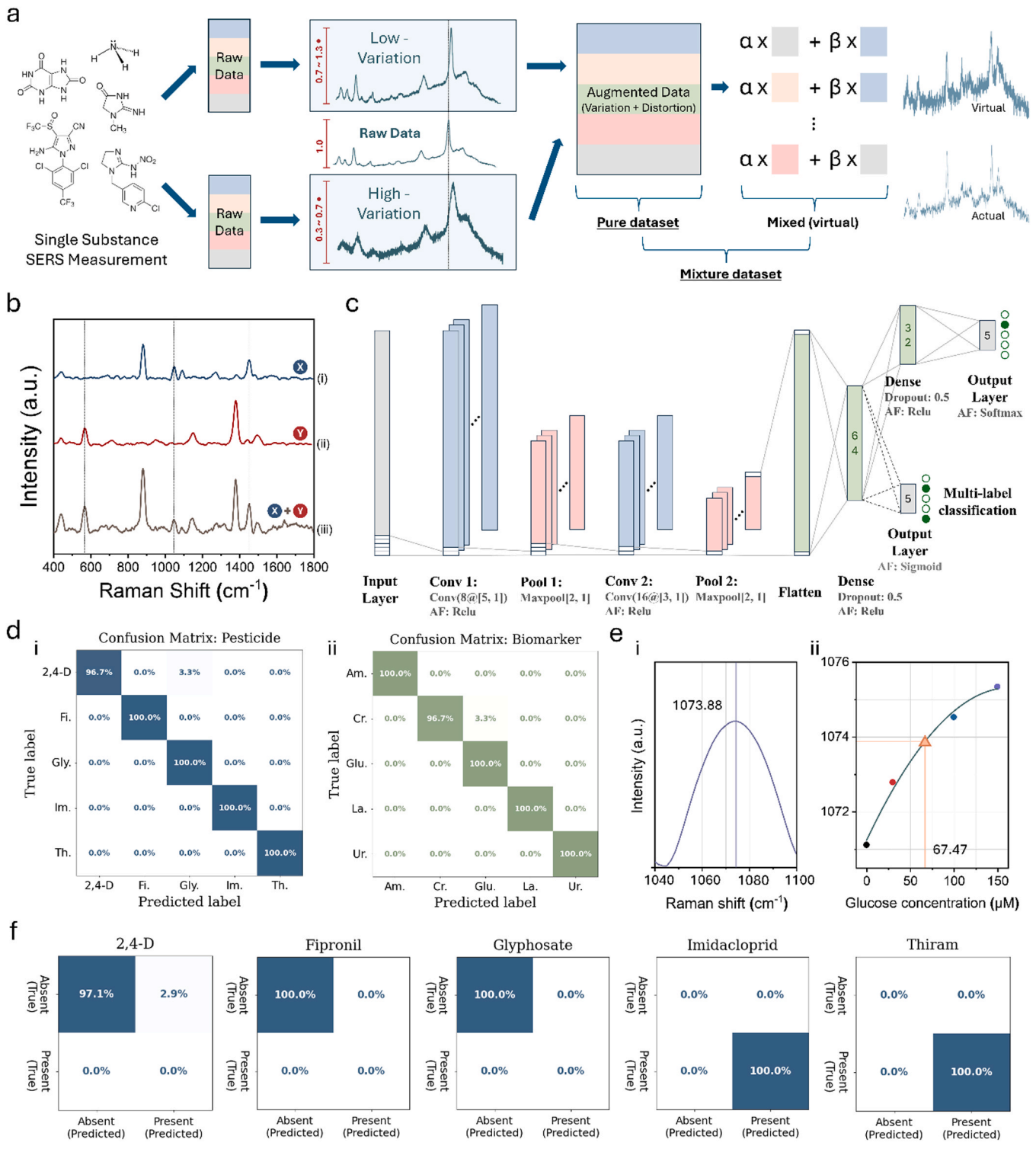


Fig. 5. Deep-learning analysis of single- and multi-analyte SERS spectra on the MS + CT + S platform. a, Two-branch data augmentation pipeline that expands each measured single-analyte spectrum into low-variation and high-variation training samples; for the multi-label classifier, virtual mixtures are further generated by linear superposition of the augmented spectra and shown alongside the experimentally measured mixture distribution. **b,** Spectrum-level validation of the linear superposition assumption: experimentally measured spectra of (i) imidacloprid, (ii) thiram, and (iii) a 1:1 imidacloprid + thiram mixture. **c,** Architecture of the 1D-CNN classifiers, sharing a convolutional backbone with task-specific fully connected layers and output activations. White squares represent individual convolutional kernels. **d,** Confusion matrices of the single-label classifier on held-out test spectra: (i) five-class pesticide panel (Fi., fipronil; Gly., glyphosate; Im., imidacloprid; Th., thiram) and (ii) five-class biomarker panel (Am., ammonia; Cr., creatinine; Glu., glucose; La., lactate; Ur., uric acid), with a worst-class test accuracy of 96.7% in both panels. **e,** Glucose concentration estimation on a 4-MPBA-functionalised Ag surface. (i) For a single spectrum of a 65 μM glucose reference, the 4-MPBA ring-breathing peak is located at 1073.88 cm^{-1} . (ii) The regression model returns 67.47 μM for this single measurement, a 3.8% relative error from the nominal value. **f,** Per-class one-vs-rest confusion matrices of the multi-label classifier on the 35 experimentally acquired thiram + imidacloprid mixture spectra (loading ratios of 1:1, 1:2 and 1:4 and the R6G-added condition); the results for all 105 binary and ternary mixture spectra are listed in Supplementary Table 6, and every constituent analyte was identified in all spectra without exposure to experimentally measured mixtures during training.

during training. The single-label and multi-label networks were kept separate because their training distributions and decision targets are fundamentally different. The multi-label network is exposed predominantly to mixture spectra during training, so its decision capacity is allocated mainly to regions where multiple classes are partially activated, leaving less capacity for regions where only a single class is strongly activated. On single-analyte spectra it consequently reaches an average accuracy 9 %age points below that of the dedicated single-label classifier, which is disadvantageous in targeted-quantification scenarios that assume a confident single-analyte output, such as the glucose concentration regression described earlier. The single-label classifier therefore covers the targeted-quantification scenario with a prespecified analyte, while the multi-label classifier covers the screening scenario for unknown mixtures. Because the single-label classifier is trained on about 2.5×10^3 augmented spectra, compared with about 1.2×10^5 for the multi-label classifier, it is also the faster model to train and to update, which makes it the more economical choice whenever the task is only to confirm a single component. This separation enables a practical route to multi-analyte SERS without the combinatorial cost of measuring every possible mixture composition, while retaining the precision required for targeted single-analyte quantification.

2.5. AI-SERS platform: from on-body and food-surface measurements to real-world applications

To demonstrate the practical value of the integrated platform, the MS + CT + S substrate was deployed in two field-relevant settings: on-body sweat monitoring as a flexible patch, and food-surface inspection as a contact-mode sticker (Fig. 6a). In both modes, backside excitation was used so that the plasmonic layer remained in conformal contact with the sample interface throughout the measurement.

For on-body sweat sensing, a multi-label 1D-CNN classifier sharing the architecture and mixture-augmentation strategy established for the pesticide model in the previous section was retrained on five sweat-relevant biomarkers: ammonia, creatinine, glucose, lactate and uric acid. The substrate was attached to the shoulder and used to collect natural perspiration after light exercise. Backside SERS spectra acquired through the transparent PDMS support reveal characteristic peaks of uric acid, lactate and creatinine on a smooth baseline (Fig. 6b-i). When these spectra are passed to the retrained classifier, the predicted class

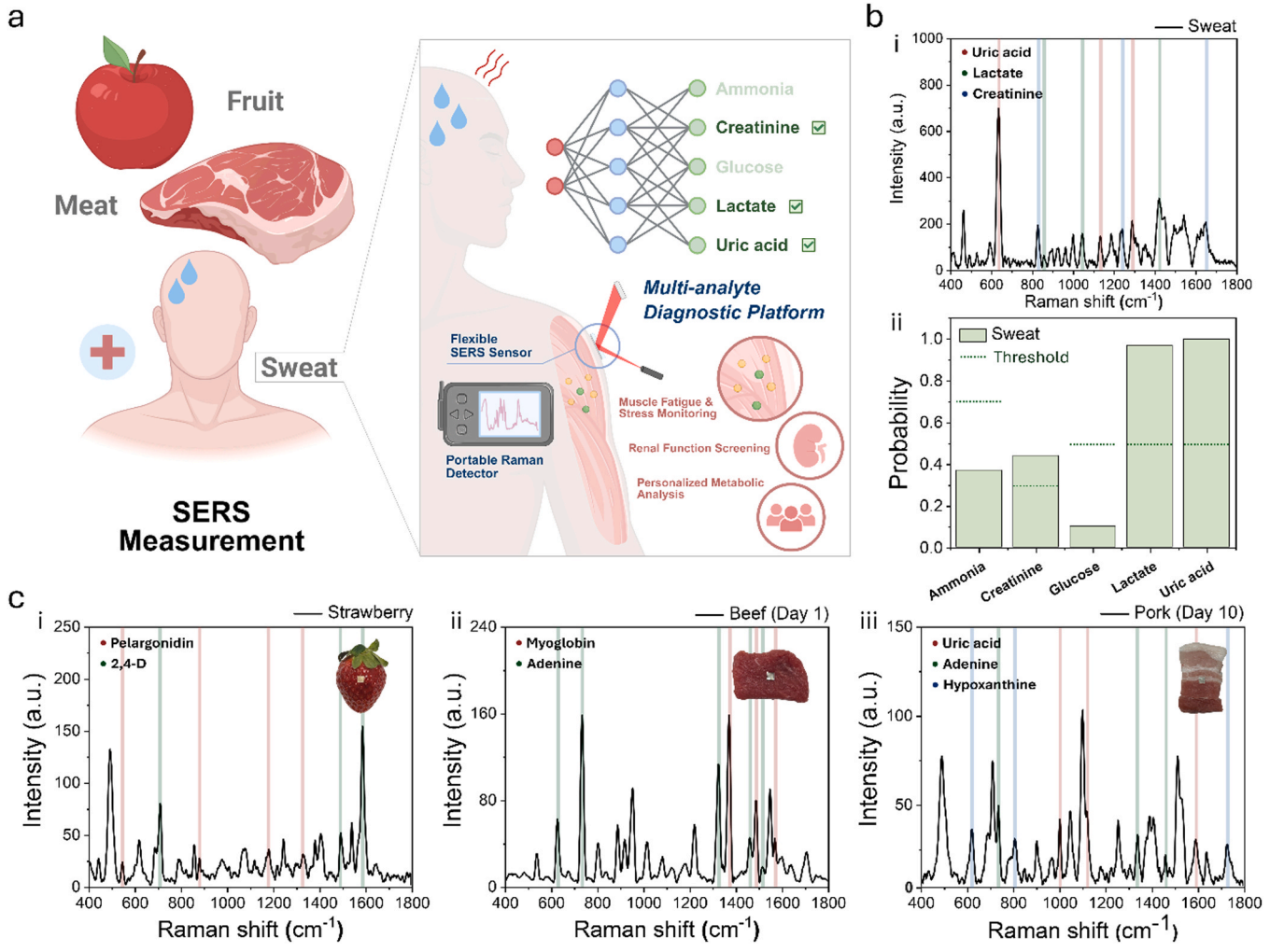


Fig. 6. Real-world deployment of the AI-SERS platform for on-body and food-surface molecular sensing. a, Application overview of the MS + CT + S substrate across representative real-world targets: fruit, meat and human sweat, together with a schematic of the skin-attached multi-analyte diagnostic patch. **b,** On-body sweat sensing. **i,** Backside SERS spectrum of natural perspiration collected from the shoulder, with characteristic peaks of uric acid, lactate and creatinine highlighted. **ii,** Multi-label classifier outputs for ammonia, creatinine, glucose, lactate and uric acid, plotted against analyte-specific decision thresholds (ammonia 0.7; creatinine 0.3; glucose, lactate and uric acid 0.5); creatinine, lactate and uric acid exceed their thresholds and are reported as positive. **c,** Food-surface sensing. **i,** Backside SERS spectrum measured on strawberry skin pre-spiked with 2,4-D, with the 2,4-D and pelargonidin peaks highlighted. **ii,** Spectrum acquired from day 1 beef sirloin, with myoglobin and adenine peaks highlighted. **iii,** Spectrum acquired from day 10 pork belly, with uric acid, adenine and hypoxanthine peaks highlighted.

probabilities for the five biomarkers are evaluated against analyte-specific decision thresholds set on the validation set (Methods; Fig. 6b-ii). Creatinine, lactate and uric acid exceed their respective thresholds and are reported as positive, while ammonia and glucose remain below threshold; this readout confirms that biomarkers commonly reported in human sweat can be simultaneously identified from a single backside SERS measurement. We note that the present dataset captures a single post-exercise time point rather than matched pre/post-exercise pairs, and the decision thresholds were set empirically, so absolute concentration changes cannot be quantified from this experiment alone. With additional time-resolved spectra accumulated before and after physical activity, the same framework could be extended to track concentration trajectories of lactate, creatinine and uric acid, supporting downstream applications such as muscle fatigue tracking, stress monitoring, renal function screening and personalized metabolic analysis.

Beyond on-body sensing, the same substrate is applicable to a wide range of food surfaces, including fresh produce and animal-derived products that share the requirement of conformal, label-free contact measurement. For surface pesticide screening, the substrate was placed in contact mode on a strawberry skin pre-spiked with 2,4-dichlorophenoxyacetic acid (2,4-D), a representative herbicide whose residue on produce is regulated worldwide. Backside SERS spectra simultaneously resolve the characteristic peaks of 2,4-D and pelargonidin, the natural anthocyanin pigment of the strawberry skin (Fig. 6c-i). This co-detection confirms that the substrate operates on rough, wet biological surfaces, and indicates that augmenting the training set with mixture spectra of target pesticides and matrix constituents could extend the same classifier to true multi-component readout on food surfaces in future work.

To illustrate the breadth of accessible food matrices, the same contact-mode protocol was applied to animal-derived products. On day 1 beef sirloin, backside SERS spectra exhibit myoglobin and adenine peaks (Fig. 6c-ii), consistent with the heme protein and nucleotide content of fresh muscle tissue stored at 4 °C. For pork belly, spectra were acquired on both day 1 and day 10 of refrigerated storage at 4 °C: the day 1 spectrum (Supplementary Fig. 11) shows adenine together with a weak hypoxanthine feature that is already present in fresh muscle [74], whereas after ten days of storage the hypoxanthine and uric acid peaks become markedly more pronounced and the relative adenine intensity decreases (Fig. 6c-iii). This relative shift is consistent with the established conversion of adenine-related nucleotides into hypoxanthine, xanthine and uric acid during purine degradation in refrigerated muscle as spoilage progresses [81,82]. A meat freshness model could be developed in future work by accumulating a sufficient library of pure-standard mixture-augmented spectra together with time-resolved samples.

Taken together, these demonstrations show that the geo-inspired hierarchical crack network supports both AI-driven multi-analyte readout, as illustrated for sweat biomarkers and surface pesticides, and rapid, label-free fingerprinting of complex food matrices, from a single conformal contact measurement. The combination of conformal backside operation, point-to-point spectral reproducibility and an extensible classifier framework positions the platform as a practical route towards on-body and on-site molecular sensing in everyday environments.

3. Conclusion

This work presents a nanogap SERS platform based on a hierarchical crack network fabricated through geo-inspired mechanothermal processing and integrated with a deep-learning classification pipeline. The primary analytical function of the platform is multiplexed molecular identification and screening based on chemically distinct SERS fingerprints. Within this framework, the concentration-dependent measurements of R6G and thiram characterize the analytical response and sensitivity of the substrate across the tested concentrations, whereas the glucose study provides an analyte-specific proof of concept for targeted concentration estimation using 4-MPBA recognition chemistry. By engineering tapered V-shaped trench geometries in an Ag/PDMS bilayer through sequential mechanical strain, cryogenic-thermal treatment and sonication, the platform achieves a ~150-fold increase in the averaged experimental SERS intensity relative to bare Ag. FDTD simulations independently show an increase in the spatially averaged electromagnetic enhancement from 1.9×10^2 for MS only to 7.5×10^3 for MS + CT + S, consistent with the processing-dependent experimental trend. The backside intensity advantage is preserved across all processing stages. Backside operation allows conformal Raman collection through the transparent PDMS support while the plasmonic layer remains attached to irregular sample surfaces. Two task-specific 1D-CNN classifiers, trained on synthetic mixture spectra generated by linear superposition and spectral augmentation from a compact single-analyte reference library, achieve a worst-class test accuracy of 96.7% for both the pesticide and the biomarker panel in single-label classification and identify every constituent analyte in 105 experimentally acquired binary and ternary mixture spectra spanning different loading ratios and an untrained interferent. As demonstrations, the platform resolves pesticide residues on fruit skin and co-existing sweat metabolites from collected perspiration sample in a single conformal backside measurement.

Despite these results, several limitations must be addressed before field deployment. First, the spectral reproducibility demonstrated here was established under well-controlled laboratory conditions; in practical on-body or food-surface use, non-uniform analyte distribution, ambient fluctuations and variable laser incidence will introduce additional variability, which could be mitigated by an internal reference standard for ratiometric correction and by machine-learning-based spectral normalization. Second, although binary and ternary mixtures at different loading ratios were resolved correctly, the augmentation pipeline assumes that mixture spectra can be approximated by linear superposition of single-analyte references, an assumption that may break down in complex matrices with competitive adsorption or concentration-dependent interactions; interaction-aware augmentation or transfer learning from a small set of measured mixtures could address this. Third, the present demonstrations are limited in scope, capturing a single post-exercise time point for sweat and spiked rather than naturally contaminated produce, so continuous monitoring and field-level validation across diverse subjects and samples remain important next steps.

Notwithstanding these challenges, the integration of scalable, lithography-free nanogap fabrication, conformal backside excitation and data-efficient deep-learning classification within a single flexible platform establishes a practical framework for multiplexed molecular sensing. By removing the need for front-side sample preparation and exhaustive mixture-by-mixture training data, the approach lowers the barrier to deploying SERS-based analysis on complex biological and food surfaces, offering a pathway toward non-invasive metabolic monitoring and on-site food-safety screening in everyday environments.

4. Materials and methods

4.1. Nanofabrication of MS + CT + S SERS substrate

4.1.1. Substrate fabrication

A polydimethylsiloxane (PDMS) elastomer and curing agent (Sylgard 184, Dow Corning Corp.) were mixed in a 10:1 wt ratio and thermally cured at 80 °C for 6 h, forming a PDMS layer with an approximate thickness of 300 μm. The cured PDMS substrate was diced into 2×1 cm^2 pieces. A silver (Ag) thin film was deposited onto the PDMS surface by ultra-high-vacuum DC magnetron sputtering at a base pressure of 9×10^{-8} Torr. Under an argon (Ar) atmosphere maintained below 2×10^{-2} Torr with a constant flow rate of 34 sccm, a 50 nm-thick Ag film was deposited at a rate of 12.6 Å s^{-1} using a 99.9%-pure Ag target operated at 20 W. Subsequently, a 1×1 cm^2 Ag thin film was patterned at the center of the diced PDMS substrate using polyimide (PI)

tape as a shadow mask.

4.1.2. Sequential mechanothermal processing

Samples were uniaxially strained up to 75% for 25 cycles using a custom stretching apparatus, immersed in liquid nitrogen for 5 min, immediately annealed at 100 °C for 20 min in air, and ultrasonicated in ethanol for 20 min (POWERSONIC 405, maximum intensity). Tensile strain was defined as $\varepsilon = (L - L_0)/L_0 \times 100\%$, where L_0 and L are the initial and stretched lengths. The rationale for each condition is provided in Supplementary Notes 2–4.

4.2. Characterization and measurement

4.2.1. Structural characterization

Surface morphologies were examined using field-emission SEM (FE-SEM, JSM-IT800, JEOL) and optical microscopy (Olympus BX41M). Cross-sectional morphologies of the V-shaped trenches, secondary cracks, and nanogaps were characterized by STEM and FIB-SEM. Structural parameters reported in Supplementary Table 2 were extracted using a combined imaging protocol: inter-trench spacing was measured from low-magnification SEM images, while the top and bottom opening widths of the V-shaped trenches were determined from high-magnification SEM and cross-sectional STEM images.

4.2.2. SERS measurement protocol

SERS spectra were acquired with a confocal Raman microscope at 633 nm excitation through a 100 × objective (NA 0.8). Unless otherwise specified, the laser power measured at the sample plane after the objective was 5.8 mW and the integration time was 10 s. The diffraction-limited spot diameter calculated as $1.22\lambda/\mathrm{NA}$ is 0.96 μm, corresponding to a spot area of 0.73 μm^2 and a power density of $\sim 8 \times 10^5$ W cm^{-2}. Spatial reproducibility was assessed by Raman mapping over a 4 × 4 mm^2 area (100 measurement points arranged in a 10 × 10 grid with a 444 μm step size) after airbrush deposition of analytes (Supplementary Fig. 10). The mapping was performed in a serpentine (zigzag) scanning pattern starting from the top-left corner: the laser scanned rightward along the first row, then leftward along the second row, alternating directions for each subsequent row. The resulting 10 × 10 array of individual spectra was merged to obtain the representative spectrum of the substrate.

4.2.3. Inter-substrate reproducibility measurements

Twenty MS + CT + S substrates were prepared independently using the standard fabrication protocol described above; one spectrum was acquired at the center of each substrate after drop casting of 50 μL of R6G (10^{-5} M) and drying under ambient conditions, and the twenty center spectra were used to compute the inter-substrate RSD at the 1361 cm^{-1} band.

4.2.4. Laser power dependence measurements

The incident laser power at the sample plane was varied using the discrete neutral-density (ND) filter settings available on the instrument, which gave 1, 2.4, 3.1, 3.7, 4.5, 5.8 and 6.5 mW (the last being the maximum available setting), as verified by a laser power meter; these values correspond to power densities of 1.4×10^5 to 8.9×10^5 W cm^{-2} for the 0.73 μm^2 spot area. All other acquisition parameters were kept identical to the standard SERS measurement conditions. At each power, five spectra were acquired at different positions of a single MS + CT + S substrate after drop casting of 50 μL of R6G (10^{-5} M), and the peak intensity at 1361 cm^{-1} in Fig. 4b is given as the mean ± standard deviation of the five spectra.

4.2.5. Glucose detection by 4-MPBA functionalization

For glucose detection, MS + CT + S substrates were immersed in a 4-mercaptophenylboronic acid (4-MPBA, Sigma-Aldrich) ethanol solution for one day to anchor 4-MPBA monolayers on the Ag surface via thiol-Ag binding. Glucose solutions (Sigma-Aldrich) at 0, 30, 100 and 150 μM in deionized water were then drop-cast as 50 μL aliquots onto the functionalized substrates and dried under ambient conditions. Raman spectra were acquired with 633 nm laser excitation over the 400–1800 cm^{-1} range, with the 1040–1100 cm^{-1} region used to track the position of the 4-MPBA ring-breathing peak, which shifts to higher wavenumbers upon boronate-ester formation between the 4-MPBA boronic-acid group and the diol moiety of glucose [74]. When a measured spectrum was classified as glucose by the single-label classifier, the peak position in the 1070–1080 cm^{-1} region was passed to a second-order calibration curve fitted to peak shift versus concentration to estimate the glucose concentration.

4.3. Materials and reagents

4.3.1. Analyte preparation and concentration series

R6G and thiram (both from Sigma-Aldrich) were each dissolved in ethanol to prepare 10^{-4} M stock solutions, which were then serially diluted in ethanol to obtain concentration series spanning 10^{-4} to 10^{-7} M. For the reference analyte panel, imidacloprid, 2,4-dichlorophenoxyacetic acid (2,4-D) and fipronil were dissolved in ethanol, while uric acid, lactate, creatinine, ammonia and glyphosate were dissolved in deionized water, each at 10^{-3} M (all reagents from Sigma-Aldrich). All R6G, thiram and reference solutions were applied to the MS + CT + S substrate by drop casting 50 μL of solution at the substrate center and drying under ambient conditions before measurement. For the concentration series in Fig. 4c, five spectra were acquired at different positions of the substrate at each concentration, and the peak intensities are given as the mean ± standard deviation.

4.3.2. Mixture sample preparation

Binary and ternary pesticide mixtures for the evaluation of the multi-label classifier were prepared on MS + CT + S substrates by sequential drop casting of the 10^{-3} M single-analyte solutions described above, each 50 μL application being dried under ambient conditions before the next. The nominal loading ratio denotes the number of applications of each component: thiram:imidacloprid = 1:1, 1:2 and 1:4, thiram:2,4-D = 1:3 and thiram:imidacloprid:2,4-D = 1:2:3, with thiram, the strongest SERS scatterer of the panel, kept as the minority component. For the interferent condition, 50 μL of R6G (10^{-6} M) was additionally drop-cast onto 1:1 thiram + imidacloprid samples and spectra were acquired at five positions with different background levels. Twenty spectra were acquired for the 1:1 thiram + imidacloprid mixture, five for each of the other thiram + imidacloprid conditions and 35 for each of the thiram + 2,4-D and ternary mixtures, giving 105 spectra in total; none of them was used for training, validation or threshold selection.

4.4. Numerical analysis

4.4.1. FDTD simulations

Three-dimensional simulations were performed using Lumerical FDTD (Ansys). Top-view models were constructed by importing binary masks of the experimental SEM morphologies, and cross-sectional models of the V-shaped trench were parametrized with a 100 nm top opening and a trench depth of 30–45 nm. Plane-wave excitation at 633 nm was launched at normal incidence from either the air side or the PDMS side. The optical properties of Ag were taken from Johnson and Christy [83] in the spectrum range from 400 to 2500 nm. A refractive index of $n = 1.41$ was used for PDMS. Periodic and perfectly matched-layer boundary conditions were applied as appropriate for the simulation geometry, with a 1–2 nm mesh in the gap region. Full simulation parameters are provided in Supplementary Note 5.

4.5. Machine-learned classification

4.5.1. Spectral processing

For visualization of the SERS spectra, baseline correction and smoothing were applied before plotting.

4.5.2. Data augmentation

For the single-label classifier, the measured spectra assigned to the training subset for each analyte were expanded 50-fold through a two-branch augmentation pipeline; for the multi-label classifier, the measured single-analyte spectra of the training and validation subsets for each analyte were expanded 80-fold using the same pipeline. Low-variation samples were generated by mild intensity scaling (×0.7–1.3), small Raman shift perturbation within 5 cm^{-1} , and small-amplitude Gaussian noise. High-variation samples were generated using the same operations over wider ranges, including intensity attenuation (×0.3–0.7), larger Raman shifts, peak broadening, and larger-amplitude Gaussian noise. Prior to augmentation, every spectrum was interpolated onto a common 1 cm^{-1} -spaced axis (400–1800 cm^{-1} for the single-label classifier and 400–1700 cm^{-1}, the range covered by every measured spectrum, for the multi-label classifier) and L2-normalized; for the multi-label classifier, each L2-normalized spectrum was then converted to its Savitzky-Golay first derivative (window of 11 points, third-order polynomial) and L2-normalized again, so that augmentation and mixture synthesis operated on derivative spectra, and all network inputs were subsequently standardized to zero mean and unit variance using statistics computed on the training set. For the multi-label classifier, virtual mixture spectra were further synthesized by linear superposition of the augmented single-analyte spectra for every pairwise combination of the five target analytes, with mixing coefficients α drawn from three regimes ($\alpha = 0.05$–0.20 for weakly visible components, 0.30–0.70 for ambiguous mixtures, and 0.80–0.95 for dominant components). For the ternary combination of thiram, imidacloprid and 2,4-D, ternary synthetic spectra were additionally generated by superposing three augmented single-analyte spectra with weights drawn from a Dirichlet distribution and rescaled to lie between 0.05 and 0.90.

4.5.3. Dataset partitioning

For the single-label classifier, the 50 measured spectra per analyte were split at the level of the original measurements into training, validation and test subsets, and augmentation was applied only to the training subset, so that validation and test evaluation used exclusively non-augmented measured spectra. For the multi-label classifier, the 50 measured spectra per analyte were likewise split at the level of the original measurements into 40 training and 10 validation spectra before augmentation, and the augmented single-analyte spectra and synthetic mixtures used for training and for validation were generated exclusively from the respective subsets, so that no augmented or synthetic spectrum in the validation set derived from a measurement used for training (3200 augmented spectra per analyte and 3200 synthetic mixtures per analyte pair and for the ternary combination from the training subset; 800 of each from the validation subset). Because mixture spectra were the primary target of the multi-label task, synthetic mixtures were oversampled threefold and additionally weighted threefold in the loss relative to the single-analyte spectra to increase their contribution during training. Held-out testing was performed exclusively on the 105 experimentally acquired binary and ternary mixture spectra described above, which were not used for training, validation or threshold selection, and no synthetic or augmented spectrum was included in the test set (Supplementary Table 7).

4.5.4. Network architecture

Both classifiers were built on a 1D-CNN backbone consisting of two 1D convolutional layers (eight and sixteen filters with kernel sizes of 5 and 3, respectively, each followed by max-pooling) and a flatten layer. The single-label classifier appended two fully connected layers (64 and 32 units, dropout 0.5) and a softmax output. The multi-label classifier appended one fully connected layer (64 units, dropout 0.5) and a sigmoid output that returned the probability of each analyte being present independently of the others.

4.5.5. Training configuration

All networks were implemented in TensorFlow and trained with the Adam optimizer (learning rate 1×10^{-3}, default $\beta_1 = 0.9$ and $\beta_2 = 0.999$, no learning-rate schedule) at a batch size of 128. The single-label classifiers used the categorical cross-entropy loss and the multi-label classifier used the binary cross-entropy loss with sigmoid outputs; both were trained for up to 200 epochs with early stopping on the validation loss (patience of 50 epochs for the single-label classifiers and 10 epochs for the multi-label classifier) and restoration of the weights from the epoch with the lowest validation loss. Overfitting was controlled by dropout (0.5) after each fully connected layer, by early stopping, by the noise, shift and broadening operations of the augmentation pipeline, by the measurement-level partitioning that keeps the validation data free of augmented versions of any training measurement, and by evaluating exclusively on measured spectra. For the multi-label classifier, class-specific decision thresholds were selected on the validation set by scanning values from 0.1 to 0.9 and adopting, for each class, the threshold with the highest F1 score (Supplementary Note 7). The single-label classifiers comprise 359,109 trainable parameters and the multi-label classifier 331,589; all hyperparameters are listed in Supplementary Table 8.

4.5.6. Sweat biomarker classifier

A multi-label 1D-CNN classifier sharing the architecture and mixture-augmentation strategy established for the pesticide model was retrained on pure-standard SERS spectra of ammonia, creatinine, glucose, lactate and uric acid, augmented with computationally generated mixture spectra. Analyte-specific decision thresholds (ammonia 0.7; creatinine 0.3; glucose, lactate and uric acid 0.5) were set empirically on the validation set.

4.5.7. Spectral assignment of non-trained analytes

The 2,4-D signal on strawberry skin was identified by the pesticide classifier. Pelargonidin (strawberry), myoglobin and adenine (beef sirloin), and adenine, hypoxanthine and uric acid (pork belly), which were not included in any training set, were assigned manually by comparison with reference Raman spectra of the corresponding pure standards.

4.6. On-body and real-sample evaluation

4.6.1. On-body sweat measurement

Before substrate attachment, the shoulder skin was wiped with deionized water and air-dried. A 1×1 cm^2 MS + CT + S patch was conformally attached to the cleaned area without additional adhesive. Each participant performed light exercise at room temperature until natural perspiration was visible at the patch interface, after which Raman spectra were acquired in situ through the transparent PDMS support under the conditions described in SERS measurement protocol. Each spectrum was acquired from a single point measurement without spectral averaging.

4.6.2. Strawberry sample preparation

Strawberries (cultivar Seolhyang) were purchased from Nonghyup Agribusiness Group and stored at 4 °C in their original packaging until use. All measurements were performed within 10 h of purchase. Immediately before measurement, the outer skin of each strawberry was rinsed with deionized water and air-dried, and a controlled volume of 10^{-3} M 2,4-D in ethanol was deposited onto the skin and allowed to dry. The MS + CT + S substrate was placed on top of the spiked skin surface

without applied pressure, and Raman spectra were acquired in situ through the PDMS support. Each spectrum was acquired from a single point measurement without spectral averaging.

4.6.3. Meat sample preparation

Beef sirloin and pork belly were purchased from Samjung Food Co., Ltd. and stored at 4 °C in covered Petri dishes from day 1 to day 10 after the slaughter date indicated on the package, without surface drying or any other pre-treatment. On each measurement day, the MS + CT + S substrate was placed on top of the meat surface inside the Petri dish without applied pressure, and Raman spectra were acquired in situ through the PDMS support. Each spectrum was acquired from a single point measurement without spectral averaging.

Author contributions

S.L., Y.K., J.A., and W.L. conceived the idea and designed the project. Y.K., J.A., and W.L. supervised the overall research. S.L., J.L., and C.C. designed and fabricated the SERS substrate. S.L., J.L., Y.K. performed the characterization and FDTD simulations. M.K., S.R., and J.Y. conducted the on-body and real-sample evaluation. S.L., J.L., M.K., C.C., Y. K., J.A., and W.L. evaluated the experiments and contributed valuable ideas. S.L., J.L., M.K., Y.K., J.A., and W.L. wrote the manuscript. All authors discussed the results and commented on the manuscript.

CRediT authorship contribution statement

Seunghyun Lee: Writing – original draft, Methodology, Investigation, Conceptualization. **Minki Kim:** Writing – original draft, Visualization, Software, Data curation. **Joonho Lee:** Writing – original draft, Methodology, Formal analysis, Conceptualization. **Changhyun Choi:** Investigation, Formal analysis. **Seungyeop Ryu:** Visualization, Methodology, Data curation. **Jinhyeok Yang:** Software, Resources, Data curation. **Yeonhong Kim:** Writing – original draft, Visualization, Project administration, Formal analysis, Conceptualization. **Junseong Ahn:** Writing – review & editing, Validation, Supervision, Project administration, Funding acquisition. **Wooyoung Lee:** Supervision, Resources, Project administration, Funding acquisition.

Code availability

The custom codes for machine-learned classification used in this study are provided as Supplementary Data 2 with its description.

Declaration of Competing Interest

The authors declare that they have no known competing financial interests or personal relationships that could have appeared to influence the work reported in this paper.

Acknowledgements

This work was supported by the National Research Foundation of Korea (NRF), funded by the Korean government (Ministry of Science and ICT, MSIT) (No. RS-2022-NR068261, National Core Materials Research Center, Platform Type). Additional support was provided by the Commercialization Promotion Agency for R&D Outcomes (COMPA), funded by MSIT (No. RS-2026–25529181, RS-2026–25541162) J. Lee acknowledges support from the Korea Institute for Advancement of Technology (KIAT) through a grant funded by the Korean Government (MOTIE) (RS-2025–02215617, HRD Program for Industrial Innovation). This work was also supported by the National Research Foundation of Korea (NRF) grant funded by the Korean government (MSIT, No. RS-2025–00523026) and by Basic Science Research Program through the National Research Foundation of Korea (NRF) funded by the Ministry of Education (RS-2026–25571231).

Appendix A. Supporting information

Supplementary data associated with this article can be found in the online version at doi:10.1016/j.snb.2026.141052.

Data availability

Data will be made available on request.

References

[1] Y. Wang, et al., Wearable Plasmonic-Metasurface Sensor for Noninvasive and Universal Molecular Fingerprint Detection on Biointerfaces, Sci. Adv. 7 (2021). https://www.science.org.
[2] V.T.N. Linh, et al., Flexible surface-enhanced Raman scattering substrates toward sampling approaches for on-site sensing and diagnosis applications, Appl. Spectrosc. Rev. 59 (2024) 90–123, https://doi.org/10.1080/05704928.2023.2181818.
[3] L. Xie, et al., State of the art in flexible SERS sensors toward label-free and onsite detection: from design to applications, Nano Res. 15 (2022) 4374–4394, https://doi.org/10.1007/s12274-021-4017-4.
[4] S. Park, J. Lee, H. Ko, Transparent and Flexible Surface-Enhanced Raman Scattering (SERS) Sensors Based on Gold Nanostar Arrays Embedded in Silicon Rubber Film, ACS Appl. Mater. Interfaces 9 (2017) 44088–44095.
[5] L. Song, J. Chen, B.Bin Xu, Y. Huang, Flexible Plasmonic Biosensors for Healthcare Monitoring: Progress and Prospects, ACS Nano 15 (2021) 18822–18847, https://doi.org/10.1021/acsnano.1c07176.
[6] L. Liu, et al., Highly Scalable, Wearable Surface-Enhanced Raman Spectroscopy, Adv. Opt. Mater. 10 (2022).
[7] X. Gui, et al., Wearable and Flexible Nanoporous Surface-Enhanced Raman Scattering Substrates for Sweat Enrichment and Analysis, ACS Appl. Nano Mater. 6 (2023) 11049–11060.
[8] R. Peng, et al., Recent Development and Applications of Stretchable SERS Substrates, Nanomaterials 13 (2023), https://doi.org/10.3390/nano13222968.
[9] S. Luo, et al., Large Area Patterning of Highly Reproducible and Sensitive SERS Sensors Based on 10-nm Annular Gap Arrays, Nanomaterials 12 (2022).
[10] S. Fruncillo, X. Su, H. Liu, L.S. Wong, Lithographic Processes for the Scalable Fabrication of Micro- And Nanostructures for Biochips and Biosensors, ACS Sens. 6 (2021), https://doi.org/10.1021/acssensors.0c02704.
[11] N. Pazos-Pérez, et al., Highly uniform SERS substrates formed by wrinkle-confined drying of gold colloids, Chem. Sci. 1 (2010) 174–178.
[12] S. Hwang, D. Jung, H.J. Kim, S.H. Lim, H.N. Lee, Facile fabrication of Au thin film substrates with crack-like nanogaps for surface-enhanced Raman spectroscopy, Thin Solid. Films 798 (2024).
[13] T. Moon, et al., Adaptive Gap-Tunable Surface-Enhanced Raman Spectroscopy, Nano Lett. 24 (2024) 3777–3784.
[14] K. Sanger, et al., Large-Scale, Lithography-Free Production of Transparent Nanostructured Surface for Dual-Functional Electrochemical and SERS Sensing, ACS Sens. 2 (2017) 1869–1875.
[15] V. Awasthi, P. Malik, R. Goel, P. Srivastava, S.K. Dubey, Nanogap-Rich Surface-Enhanced Raman Spectroscopy-Active Substrate Based on Double-Step Deposition and Annealing of the Au Film over the Back Side of Polished Si, ACS Appl. Mater. Interfaces 15 (2023) 10250–10260.
[16] B.L. Darby, E.C. Le Ru, Competition between molecular adsorption and diffusion: Dramatic consequences for SERS in colloidal solutions, J. Am. Chem. Soc. 136 (2014) 10965–10973.
[17] J. Plou, M. Charconnet, I. García, J. Calvo, L.M. Liz-Marzán, Preventing Memory Effects in Surface-Enhanced Raman Scattering Substrates by Polymer Coating and Laser-Activated Deprotection, ACS Nano 15 (2021) 8984–8995.
[18] R. Li, R.G. Petschek, J. Han, M. Huang, Effect of different analyte diffusion/adsorption protocols on SERS signals, Mol. Phys. 116 (2018) 1844–1850.
[19] N.P.W. Pieczonka, R.F. Aroca, Inherent complexities of trace detection by surface-enhanced Raman scattering, ChemPhysChem 6 (2005) 2473–2484, https://doi.org/10.1002/cphc.200500112.
[20] Y. Huang, X. Wang, K. Lai, Y. Fan, B.A. Rasco, Trace analysis of organic compounds in foods with surface-enhanced Raman spectroscopy: Methodology, progress, and challenges, Compr. Rev. Food Sci. Food Saf. 19 (2020) 622–642, https://doi.org/10.1111/1541-4337.12531.
[21] T. Rojalin, D. Antonio, A. Kulkarni, R.P. Carney, Machine Learning-Assisted Sampling of Surfance-Enhanced Raman Scattering (SERS) Substrates Improve Data Collection Efficiency, Appl. Spectrosc. 76 (2022) 485–495.
[22] M. Kim, et al., Surface-functionalized SERS platform for deep learning-assisted diagnosis of Alzheimer's disease, Biosens. Bioelectron. 251 (2024).
[23] E.X. Tan, et al., Transfer Learning-Assisted SERS: Predicting Molecular Identity and Concentration in Mixtures Using Pure Compound Spectra, Angew. Chem. Int. Ed. 64 (2025).
[24] X. Zhang, et al., Multicomponent Simultaneous Identification Network (MSINet): An Advanced Deep Learning Model for Boosting Multiplex SERS Detection in Untreated Real Samples, Anal. Chem. 98 (2026) 9672–9682.
[25] S.M. Quarin, D. Vang, R.I. Dima, G. Stan, P. Strobbia, AI in SERS sensing moving from discriminative to generative, npj Biosensing 2 (2025).

[26] A.R. Flanagan, D. Dalal, F.G. Glavin, Exploring Generative Artificial Intelligence and Data Augmentation Techniques for Spectroscopy Analysis, Chem. Rev. 125 (2025) 6130–6155, https://doi.org/10.1021/acs.chemrev.4c00815.
[27] D. Park, D. Lee, M.H. Moghaddam, D.S. Kim, Trench Formation under the Tunable Nanogap: Its Depth Depends on Maximum Strain and Periodicity, Micromachines 14 (2023).
[28] Q. Ding, et al., Gap-enhanced V-shaped SERS substrate for multiplex trace dye pollutants detection in river water, Appl. Surf. Sci. 706 (2025).
[29] P.L. Stiles, J.A. Dieringer, N.C. Shah, R.P. Van Duyne, Surface-enhanced Raman spectroscopy, Annu. Rev. Anal. Chem. 1 (2008) 601–626, https://doi.org/10.1146/annurev.anchem.1.031207.112814.
[30] M.S. Hu, A.G. Evans, The cracking on and decohesion of thin films ductile substrates, Acta Metall. 37 (1989).
[31] M.D. Thouless, Crack Spacing in Brittle Films on Elastic Substrates, J. Am. Ceram. Soc. 73 (1990) 2144–2146.
[32] S. Frank, U.A. Handge, S. Olliges, R. Spolenak, The relationship between thin film fragmentation and buckle formation: Synchrotron-based in situ studies and two-dimensional stress analysis, Acta Mater. 57 (2009) 1442–1453.
[33] N. Bowden, S. Brittain, A.G. Evans, J.W. Hutchinson, G.M. Whitesides, Spontaneous formation of ordered structures in thin films of metals supported on an elastomeric polymer, Nature 393 (1998) 146–149.
[34] B.C. Kim, et al., Guided fracture of films on soft substrates to create micro/nano-feature arrays with controlled periodicity, Sci. Rep. 3 (2013).
[35] K.L. Mills, X. Zhu, S. Takayama, M.D. Thouless, The mechanical properties of a surface-modified layer on polydimethylsiloxane, J. Mater. Res. 23 (2008) 37–48.
[36] J. Lee, W. Shim, E. Lee, J. Noh, W. Lee, Highly Mobile Palladium Thin Films on an Elastomeric Substrate: Nanogap-Based Hydrogen Gas Sensors, Angew. Chem. Int. Ed. 50 (2011) 5301–5305.
[37] B. Jang, W. Kim, M.J. Song, W. Lee, Thermal stability of the sensing properties in H2 sensors composed of Pd nanogaps on an Elastomeric Substrate, Sens. Actuators B Chem. 240 (2017) 186–192.
[38] H.-H. Yu, J.W. Hutchinson, Delamination of Thin Film Strips, Thin Solid. Films 423 (2003).
[39] N. Padhye, D.M. Parks, B.L. Trout, A.H. Slocum, A New Phenomenon: Sub-T g, Solid-State, Plasticity-Induced Bonding in Polymers, Sci. Rep. 7 (2017).
[40] G. Zhang, Y. Sun, B. Qian, H. Gao, D. Zuo, Experimental study on mechanical performance of polydimethylsiloxane (PDMS) at various temperatures, Polym. Test. 90 (2020).
[41] W.W. Tooley, S. Feghhi, S.J. Han, J. Wang, N.J. Sniadecki, Thermal fracture of oxidized polydimethylsiloxane during soft lithography of nanopost arrays, J. Micromech. Microeng. 21 (2011).
[42] J. Thurn, R.F. Cook, Stress hysteresis during thermal cycling of plasma-enhanced chemical vapor deposited silicon oxide films, J. Appl. Phys. 91 (2002) 1988–1992.
[43] K.S. Suslick, Sonochemistry, Science (1979) 247 (1990) 1439–1445.
[44] C.E. Brennen, Cavitation and Bubble Dynamics, Oxford University Press, 1995.
[45] M.S. Plesset, R.B. Chapman, Collapse of an initially spherical vapour cavity in the neighbourhood of a solid boundary, J. Fluid. Mech. 47 (1971) 283–290.
[46] F. Vaz, et al., Mechanical characterization of reactively magnetron-sputtered TiN films, Surf. Coat. Technol. 174 (2003) 375–382.
[47] M. Hommel, O. Kraft, Deformation behavior of thin copper films on deformable substrates, Acta Mater. 49 (2001). www.elsevier.com/locate/actamat.
[48] Z. Cedric Xia, J.W. Hutchinson, Crack patterns in thin films, J. Mech. Phys. Solids 48 (2000) 1107–1131.
[49] L.B. Freund, S. Suresh, Thin Film Materials: Stress, Defect Formation and Surface Evolution, Cambridge university press, 2004.
[50] C. Kim, et al., Large-scale nanoporous metal-coated silica aerogels for high SERS effect improvement, Sci. Rep. 8 (2018).
[51] Y. Kim, P. Gupta, K. Kim, Controlling the Multiscale Topography of Anodized Aluminum Oxide Nanowire Structures for Surface-Enhanced Raman Scattering and Perfect Absorbers, ACS Appl. Mater. Interfaces 12 (2020) 58390–58402.
[52] F. Schneider, J. Draheim, R. Kamberger, U. Wallrabe, Process and material properties of polydimethylsiloxane (PDMS) for Optical MEMS, Sens. Actuators A Phys. 151 (2009) 95–99.
[53] A. Srinivasan, B. Czapla, J. Mayo, A. Narayanaswamy, Infrared dielectric function of polydimethylsiloxane and selective emission behavior, Appl. Phys. Lett. 109 (2016).
[54] M.I. Stockman, Nanofocusing of optical energy in tapered plasmonic waveguides, Phys. Rev. Lett. 93 (2004).
[55] D.K. Gramotnev, S.I. Bozhevolnyi, Plasmonics beyond the diffraction limit, Nat. Photonics 4 (2010) 83–91, https://doi.org/10.1038/nphoton.2009.282.
[56] H. Choi, et al., Compressing surface plasmons for nano-scale optical focusing, Opt. Express 17 (2009) 7519–7524.
[57] H.T. Miyazaki, Y. Kurokawa, Squeezing visible light waves into a 3-nm-thick and 55-nm-long plasmon cavity, Phys. Rev. Lett. 96 (2006).
[58] H. Choo, et al., Nanofocusing in a metal-insulator-metal gap plasmon waveguide with a three-dimensional linear taper, Nat. Photonics 6 (2012) 838–844.
[59] A.I. Pérez-Jiménez, D. Lyu, Z. Lu, G. Liu, B. Ren, Surface-enhanced Raman spectroscopy: Benefits, trade-offs and future developments, Chem. Sci. 11 (2020) 4563–4577, https://doi.org/10.1039/d0sc00809e.
[60] L. Mandrile, A.M. Giovannozzi, A. Sacco, G. Martra, A.M. Rossi, Flexible and transparent substrates based on gold nanoparticles and TiO2 for in situ bioanalysis by surface-enhanced raman spectroscopy, Biosensors 9 (2019).
[61] J. Wang, et al., Development of a Novel Colorimetric pH Biosensor Based on A-Motif Structures for Rapid Food Freshness Monitoring and Spoilage Detection, Biosensors 14 (2024).
[62] C. Viets, W. Hill, Laser power effects in SERS spectroscopy at thin metal films, J. Phys. Chem. B 105 (2001) 6330–6336.
[63] Y. Zhao, et al., Enhanced SERS stability of R6G molecules with monolayer graphene, J. Phys. Chem. C. 118 (2014) 11827–11832.
[64] M. Barelli, G. Ferrando, M.C. Giordano, F. Buatier De Mongeot, Wavelength-dependent plasmonic photobleaching of dye molecules by large-area Au nanostripe arrays, ACS Appl. Nano Mater. 5 (2022) 3470–3479.
[65] A. Merlen, F. Lagugné-Labarthet, E. Harté, Surface-enhanced Raman and fluorescence spectroscopy of dye molecules deposited on nanostructured gold surfaces, J. Phys. Chem. C. 114 (2010) 12878–12884.
[66] J.H. Kim, et al., Photothermal heating property of gold nanoparticle loaded substrates and their SERS response, Colloids Surf. A Physicochem. Eng. Asp. 498 (2016) 20–29.
[67] T. Wang, P. Xiao, L. Ye, P. Zhu, L. Zhuang, Coupling Au-loaded magnetic frameworks to photonic crystal for the improvement of photothermal heating effect in SERS, RSC Adv. 13 (2023) 5002–5012.
[68] W.W. Yu, I.M. White, A simple filter-based approach to surface enhanced Raman spectroscopy for trace chemical detection, Analyst 137 (2012) 1168–1173.
[69] A. Haddad, M.A. Comanescu, O. Green, T.A. Kubic, J.R. Lombardi, Detection and Quantitation of Trace Fentanyl in Heroin by Surface-Enhanced Raman Spectroscopy, Anal. Chem. 90 (2018) 12678–12685.
[70] N. Ha Anh, et al., Gold nanoparticles-based SERS nanosensor for thiram and chloramphenicol monitoring in food samples: Insight into effects of analyte molecular structure on their sensing performance and signal enhancement, Appl. Surf. Sci. 584 (2022).
[71] Y. Yang, et al., A laser-engraved wearable sensor for sensitive detection of uric acid and tyrosine in sweat, Nat. Biotechnol. 38 (2020) 217–224.
[72] M. Bariya, H.Y.Y. Nyein, A. Javey, Wearable sweat sensors, Nat. Electron. 1 (2018) 160–171, https://doi.org/10.1038/s41928-018-0043-y.
[73] J. Heikenfeld, et al., Accessing analytes in biofluids for peripheral biochemical monitoring, Nat. Biotechnol. 37 (2019) 407–419, https://doi.org/10.1038/s41587-019-0040-3.
[74] J.H. Ha, et al., SERS Sensor Integrated in Stretchable and Antimicrobial Wrapper for Food Quality Monitoring and Preservation, Small 21 (2025).
[75] C.S. Ho, et al., Rapid identification of pathogenic bacteria using Raman spectroscopy and deep learning, Nat. Commun. 10 (2019).
[76] F. Lussier, V. Thibault, B. Charron, G.Q. Wallace, J.F. Masson, Deep learning and artificial intelligence methods for Raman and surface-enhanced Raman scattering, TrAC. - Trends Anal. Chem. 124 (2020), https://doi.org/10.1016/j.trac.2019.115796.
[77] R. Luo, J. Popp, T. Bocklitz, Deep Learning for Raman Spectroscopy: A Review, Analytica 3 (2022) 287–301.
[78] D. Yang, et al., Glucose Sensing Using Surface-Enhanced Raman-Mode Constraining, Anal. Chem. 90 (2018) 14269–14278.
[79] J.H. Ha, et al., Nanotransfer Printing of Functional Nanomaterials on Electrospun Fibers for Wearable Healthcare Applications, Adv. Funct. Mater. 34 (2024).
[80] X.H. Pham, et al., Glucose detection of 4-mercaptophenylboronic acid-immobilized gold-silver core-shell assembled silica nanostructure by surface enhanced raman scattering, Nanomaterials 11 (2021).
[81] Y.T. Liu, B.N. Lu, J.Y. Peng, Hepatoprotective activity of the total flavonoids from Rosa laevigata Michx fruit in mice treated by paracetamol, Food Chem. 125 (2011) 719–725.
[82] T. Saito, K.-I. Arai, M. Matsuyoshi, A new method for estimating the freshness of fish, Bull. Jpn. Soc. Sci. Fish. 24 (1959) 749.
[83] D. Koelling, A. Freeman, F. Mueller, P.B. Johnson, R.W. Christy, Optical Constants of the Noble Metals, Phys. Rev. Lett. 11 (1963).